

# Reduced order modelling for spatial-temporal temperature and property estimation in a multi-stage hot sheet metal forming process

Daniel Kloeser<sup>a</sup>, Juri Martschin<sup>b</sup>, Thomas Meurer<sup>a</sup>, Erman Tekkaya<sup>b</sup>

<sup>a</sup>*Chair of Automatic Control, Faculty of Engineering, Kiel University, Kiel, Germany.*

<sup>b</sup>*Institute of Forming Technology and Lightweight Components, Technische Universität Dortmund, Dortmund, Germany*

---

## Abstract

A concise approach is proposed to determine a reduced order control design oriented dynamical model of a multi-stage hot sheet metal forming process starting from a high-dimensional coupled thermo-mechanical model. The obtained reduced order nonlinear parametric model serves as basis for the design of an Extended Kalman filter to estimate the spatial-temporal temperature distribution in the sheet metal blank during the forming process based on sparse local temperature measurements. To address modeling and approximation errors and to capture physical effects neglected during the approximation such as phase transformation from austenite to martensite a disturbance model is integrated into the Kalman filter to achieve joint state and disturbance estimation. The extension to spatial-temporal property estimation is introduced. The approach is evaluated for a hole-flanging process using a thermo-mechanical simulation model evaluated using LS-DYNA. Here, the number of states is reduced from approximately 17 000 to 30 while preserving the relevant dynamics and the computational time is 1000 times shorter. The performance of the combined temperature and disturbance estimation is validated in different simulation scenarios with three spatially fixed temperature measurements.

*Keywords:* State estimation, spatial-temporal temperature estimation, model order reduction, POD, heat equation, time-varying spatial domain, disturbance estimation, Extended Kalman filter, press hardening, progressive die, hot forming.

---

## 1. Introduction

Multi-stage hot sheet metal forming enables the production of complex formed press-hardened components at high stroke rates (Belanger et al., 2017). The sheet metal blank is first heated in a furnace, then optionally pre-cooled to the desired initial forming temperature and finally formed and quenched in a sequence of tools in a transfer die (Belanger, 2016). Several different forming operations are carried out on a component before the temperature falls below a critical temperature, e.g., the martensite start temperature. Löbbe et al. (2016) presented a process design for a progressive die in which the sheet metal coil is pre-punched, then rapidly austenitized by means of induction heating and formed and quenched in several consecutive stages. A modification of this process chain is the implementation of hot stamping operations in progressive die plate forging of tailored high strength gear parts by partial resistance heating (Mori et al., 2017).

These production methods have been limited to special applications due to the partially unknown and difficult to predict interplay of thermal and mechanical influences throughout the process chain. For example, the deformation history during hot forming is affected by the microstructure development and also influences the microstructure development itself (Nikraves et al., 2012). A forming and heat treatment depending shift of the transformation point from austenite to martensite causes a change in the process chain temperature history, which affects the forming process through a change in the temperature- and microstructure-dependent flow stress (Venturato et al., 2017). Besides the thermal-mechanical interactions, there are difficult to assess service life depended process influences due to batch fluctuations and the varying

tool condition (Gracia-Escosa et al., 2017). The given complexity and the lack of suitable prediction models complicate setting and maintaining desired product properties such as geometry and hardness.

In metal forming processes, models are usually obtained using the finite element method (FEM) within the design step. The resulting models are accurate but not real-time capable due to high dimensions and nonlinearities of the system. Hence a major challenge for estimator design is to develop models of reduced complexity and dimension that are still sufficiently accurate. This can be achieved by model order reduction techniques that enable us to reduce model dimension while preserving the relevant system dynamics (see, e.g., the treatise in Antoulas (2005)). Parametric model order reduction techniques provide a suitable approximation of the full-order dynamical system over a range of parameters (see, e.g., the review in Benner et al. (2015)). This approach has been successfully applied to a broad range of applications including structural dynamics, aeroelastic models as well as electrochemical and electro-thermal applications. While different approaches can be applied to compute the reduced-order models (ROMs) subsequently projection-based model order reduction is considered using proper orthogonal decomposition (POD), which can be applied to linear as well as nonlinear models. Basis vectors used for projection in POD are typically computed using the method of snapshots (Sirovich, 1987). Benner et al. (2015) provide a rather comprehensive survey on its development, variants and selected applications. In the context of sheet metal forming the application of model order reduction techniques and in particular POD can be found, e.g., in Bolzon and Buljak (2011); Radermacher and Reese (2014) for a (quasi-static) elastoplastic mechanical problems. Böhm and Meurer (2017) compare several linear model reduction techniques for the temperature control of deep drawing tools and develop a trajectory planning and feedforward control strategy based on the obtained ROM.

To enable robust and versatile production, a closed loop control has to be employed (Allwood et al., 2016), where product properties as well as decisive process variables are measured in situ during the multi-stage forming and heat treatment process. The measurements are fed back to a controller and set by adjusting the process parameters using real-time capable models. Possible actuation parameters include the kinematics of the tool and the austenitization parameters. The influence of process parameters on product quality in a press hardening application is considered in Landgrebe et al. (2015). Related results are provided in Wang et al. (2017) by taking into account the control of dwell pressure or dwell time, respectively. In both cases the preliminary heating is not considered as control variable. Models for controlling springback (Löbbecke et al., 2015), microstructure (Löbbecke et al., 2016) and strength (Löbbecke and Tekkaya, 2018) in heat-assisted bending of sheet material in a progressive die are available. However, it is not yet possible to implement multivariable control of geometric and mechanical or microstructural properties in multi-stage hot sheet metal forming. Knowledge of the temporally and spatially varying temperature distribution of the sheet is substantial for controlling the given process chain. In particular the temperature evolution is decisive for the development of the microstructure and the deformation behaviour of the material. In order to reconstruct the spatial-temporal temperature distribution from sparsely available measurement data such as pyrometers, model-based state estimation methods are inevitable. Speicher et al. (2014) designed an extended Kalman filter (EKF) for the plate rolling process and Zheng and Li (2011) for the strip rolling, respectively. Force measurements are used in Havinga and Mandal (2017) to estimate product properties by exploiting an interpolation process model obtained from a finite element model. Herein the structured uncertainties are addressed using a bias model. Taking into account tools from robust nonlinear control the design of a robust observer in view of additive parametric uncertainties is studied in Benosman and Borggaard (2021) based on ROMs for the discretized 2D Boussinesq equations to estimate air flow and temperature distributions for heating, ventilation, and air conditioning management.

In this work, a concise approach is presented that enables us to systematically determine a ROM suitable for estimator design based on the thermo-mechanical high dimensional finite element model for a multi-stage hot forming process. The proposed approach is based on the assumption of a one-sided decoupling between the thermal and the mechanical subsystems. This results in a parametric nonlinear thermal model that is utilized for model order reduction using POD. The obtained ROM is exploited for the design of an EKF to obtain a real-time estimation of the spatial-temporal temperature distribution of the sheet metal blank during the forming process based on only a few selected local temperature measurements. This furthermore enables us to deduce temperature-dependent spatial-temporal material properties, e.g., hardness, by taking into account suitable constitutive relationships. To simplify numerical evaluation of the EKF a model

simplification involving a so-called supporting or reference trajectory is proposed to obtain a linear time-varying model as a special form of a parametric model. To account for modeling errors, e.g., thermal effects of the phase transition, and reduction errors the setup is amended by a disturbance estimation that enables us to improve the estimator performance. The developments are validated in numerical simulations for a hole-flanging process.

The paper is structured as follows. Section 2 provides the problem formulation and the classical design-oriented simulation model for the coupled thermo-plastic forming process. In Section 3 a parametric ROM is deduced, which is the starting point for the EKF design in Section 4. Herein, trajectory-oriented linearization to obtain a linear time-varying model is considered and a disturbance estimation is integrated into the EKF. The methods are evaluated in Section 5 for hole-flanging process. Section 6 concludes this paper.

## 2. Problem formulation

In the following, the multi-stage hot forming process is introduced and the necessity for an estimator to reconstruct online the spatial-temporal temperature distribution is motivated. The section concludes with a description of the fully coupled LS-DYNA simulation which is used as starting point for the model order reduction.

### 2.1. Multi-stage forming process

The multi-stage hot sheet metal forming demonstrator process illustrated in Figure 1 for a progressive die is considered subsequently as introduced in Löbbe et al. (2015). After pre-punching the coil, the sheet metal blank is homogeneously heated to the austenitizing temperature  $x_\gamma$  by a combination of inductive and conductive heating (A). In stages (B) to (D) a sequence of hole-flanging (B), combined deep drawing and stretch drawing (C) as well as die bending (D) is carried out. At the same time, quenching takes place through tool contact. Figure 1 in addition shows the process inputs and the integration of the subsequently

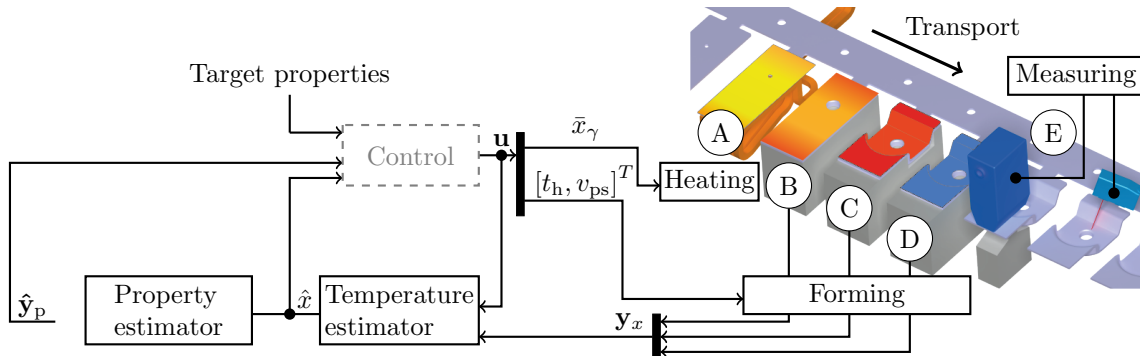


Figure 1: Schematics of estimator-based closed-loop property control in the progressive die.

determined temperature estimator to be used for both process monitoring and model-based property oriented feedback control. The process input variables that may be eventually used to control the forming process read

$$\mathbf{u} = [\bar{x}_\gamma \quad v_{ps} \quad t_h]^T. \quad (1)$$

Herein,  $\bar{x}_\gamma$  is the average austenitizing temperature, which is adjusted by an underlying control loop,  $v_{ps}$  is the punch speed, and  $t_h$  is the holding time at the bottom dead point. Obviously,  $v_{ps}$  and  $t_h$  refer to the kinematics of the ram and hence influence directly the forming steps.

In stages (A) to (D) of the real process temperature measurements  $\mathbf{y}_x(t)$  are recorded at certain time instances by thermal imaging cameras or pyrometers. Before the individual components are separated from

the strip boundary, the geometry and selected product properties  $\mathbf{y}_p(t)$  such as the microstructure are determined using a laser scanner and a 3MA-system, respectively, in stage (E).

For the design of the temperature estimation the local temperature measurements  $\mathbf{y}_x(t)$  from stages (A) to (D) serve as output injections into the estimator equations to reconstruct the spatial-temporal temperature distribution  $\hat{x}(\mathbf{z}, t)$  on the sheet metal blank. Based on this estimate we aim to assess and to evaluate the spatial-temporal distribution of key product properties  $\hat{\mathbf{y}}_p(t)$  such as hardness, yield stress or geometry that dependent on the temperature and deformation history with the property estimator. This paper focuses on the design and evaluation of the spatial-temporal robust temperature distribution and outlines the property estimation. The latter is to be combined with the property characterization considered in [Martschin et al. \(2021\)](#) towards the development of model-based property control in subsequent work.

## 2.2. Fully coupled simulation

For the numerical simulation of the sheet metal blank temperature distribution during the multi-stage process, the forming steps, the heat-exchange between sheet, tool as well as the environment and the thermo-mechanical interplay are modeled in accordance with [Hochholdinger et al. \(2011\)](#). Hereby the FE code LS-DYNA (solver: R11.1.0) is used. Tools are modeled with rigid and the blank with elasto-viscoplastic 12 node thermal thick shells. Characteristic values for convection and radiation are chosen based on [Shapiro \(2009\)](#). Martensitic stainless steel X46Cr13 is used in the simulation. Compared to conventional press hardening steels, e.g., 22MnB5, the low martensite start temperature of approximately 443 K ([Dieck et al., 2017](#)) allows a longer period of time for the multi-stage forming. The material behaviour of X46Cr13 during hot forming is modeled by a simplified adaptation of the material model Mat 248 presented by [Hippchen et al. \(2016\)](#). Temperature and strain rate-dependent flow curves and Young's modulus, thermal conductivity, heat capacity, density, and thermal expansion parameters are based on [Spittel and Spittel \(2009\)](#). Only a phase transformation from austenite to martensite is considered, since higher cooling rates are achieved in the progressive die than in air (air-hardening steel). The austenitizing of the sheet by combined inductive and conductive heating is not simulated. Prior to the transfer into the first forming stage, a fully austenitized sheet with a defined temperature distribution is assumed.

## 3. Reduced order modelling

The complexity of the LS-DYNA model is generally high and not suitable for online estimation purposes. Therefore, it is simplified in the following steps. At first, the thermal solution is separated from the mechanical solution assuming a one-sided decoupling. Secondly, ordinary differential equations are derived from the partial differential equation governing heat conduction using the finite element method so that a parameter- and state-dependent system is obtained. Third, a ROM is determined using POD.

### 3.1. One-sided decoupling of mechanical and thermal solution

To determine an explicit dynamical model of the process dynamics the fundamental assumption is imposed that the thermal solution can be separated from the mechanical solution.

**Assumption 1.** *Thermal and mechanical subsystem are coupled partially with the mechanical solution entering the thermal subsystem but not vice versa.*

This assumption simplifies the setting but introduces a modeling error that is evaluated in a simulation study in Section 5 for a hole-flanging process. Hence, only the spatial-temporal temperature distribution is determined (solved) online while the mechanical solution, that impacts the thermal simulation, is computed offline. The latter enters the thermal subsystem in terms of the parameter vector  $\mathbf{p}(\mathbf{z}, t, \mathbf{u})$ , which depends on the process conditions and hence the process inputs (1) and is composed of the following components:

- $\mathbf{u}_m(\mathbf{z}, t, \mathbf{u})$ , i.e., the deformation of the sheet metal blank with respect to the initial shape at location  $\mathbf{z}$ ;
- $l_{\text{gap}}(\mathbf{z}, t, \mathbf{u})$ , i.e. the shortest distance between the sheet metal blank and the tools at location  $\mathbf{z}$ ;

- $p_c(\mathbf{z}, t, \mathbf{u})$ , i.e., the contact pressure between the sheet metal blank and the tool at location  $\mathbf{z}$ ;
- $x_\infty(\mathbf{z}, t, \mathbf{u})$ , i.e., the contact temperature at location  $\mathbf{z}$ . This is either the ambient temperature if  $l_{\text{gap}}(\mathbf{z}, t)$  is larger than a certain threshold or the tool temperature if it is smaller.

If clear from the context we subsequently write  $\mathbf{p}$  and avoid the individual dependencies of the parameters.

### 3.2. Continuum formulation

Modelling of the temperature distribution  $x(\mathbf{z}, t)$  on the deforming sheet metal blank, whose shape at time  $t > 0$  is determined by the volume  $\Omega(t) \subset \mathbb{R}^3$  with boundary surface  $\Gamma(t)$  starting from the undeformed shape  $\Omega(0) = \Omega_0$ ,  $\Gamma(0) = \Gamma_0$ , leads to the heat equation with in general temperature dependent material properties

$$\rho c(x) \partial_t x = \nabla \cdot [\kappa(x) \nabla x] + \dot{W}(x), \quad (\mathbf{z}, t) \in \Omega(t) \times \mathbb{R}_0^+, \quad (2a)$$

$$x|_{t=0} = x_\gamma, \quad \mathbf{z} \in \Omega_0 \cup \Gamma_0, \quad (2b)$$

$$\kappa(x) \nabla x \cdot \mathbf{n} = \kappa_\infty(x, \mathbf{p}) [x_\infty - x], \quad (\mathbf{z}, t) \in \Gamma(t) \times \mathbb{R}_0^+. \quad (2c)$$

The material density  $\rho$  is assumed constant while the specific heat  $c(x(\mathbf{z}, t))$  and the thermal conductivity  $\kappa(x(\mathbf{z}, t))$  depend on the temperature distribution. The parameter  $\dot{W}(x(\mathbf{z}, t))$  refers to the induced heat and can represent, e.g., thermal effects of the phase transformation. The initial condition (2b) is given by the austenitizing temperature  $x_\gamma(\mathbf{z})$  which is set by the inductive heating process. In the following we assume that  $x_\gamma(\mathbf{z}) = \bar{x}_\gamma$ , i.e., the austenitizing temperature is homogeneously distributed. The boundary conditions (2c) in the direction of the outer normal  $\mathbf{n}(t)$  of the boundary surface  $\Gamma(t)$  are modelled by mixed boundary conditions. The values for the thermal transfer coefficient  $\kappa_\infty(x(\mathbf{z}, t), \mathbf{p})$  and the contact temperature  $x_\infty(\mathbf{z}, t, \mathbf{u})$  are determined in accordance to LS-DYNA (Livermore Software Technology Corporation, 2007; Hochholdinger et al., 2011). The parameter vector  $\mathbf{p}$  with the mechanical solution enters the formulation in two ways: (i) the time evolution of  $\Omega(t)$  depends on  $\Omega_0$ , i.e., the undeformed state, and the deformation  $\mathbf{u}_m(\mathbf{z}, t, \mathbf{u})$ , (ii) the other parameters in  $\mathbf{p}$  influence (2c).

**Remark 1** (Material derivative). *Let  $D_t$  refer to the material derivative. The system representation (2) is based on the assumption that*

$$D_t x(\mathbf{z}, t) = \partial_t x(\mathbf{z}, t) + \nabla \cdot (\mathbf{v}(\mathbf{z}, t) x(\mathbf{z}, t)) \approx \partial_t x(\mathbf{z}, t)$$

with  $\mathbf{v}(\mathbf{z}, t)$  the velocity of the domain point at  $(\mathbf{z}, t)$ . In other words we consider the rate of change observed when moving with the particle to be approximately identical with the rate of change at a fixed point. However, the setup can be easily generalized by appropriately replacing the partial differentiation  $\partial_t x(\mathbf{z}, t)$  in (2a) by  $D_t x(\mathbf{z}, t)$  and taking into account the continuity equation.

**Remark 2** (Lagrangian viewpoint). *It seems reasonable to reconsider (2) from a Lagrangian viewpoint as the time evolution of any material point due to deformation is known a-priori by means of the separation introduced in Assumption 1. This, however, introduces issues when considering the temporary contact between tool and sheet during forming. Moreover, this requires to approximate the Jacobian matrix between material and spatial coordinates online and in principle to add the differential equations determining the temporal dynamics of the material points. A comparison between the considered approach and a Lagrangian approach is not at the core of this paper and is omitted.*

### 3.3. Weak formulation

The distributed parameter description (2) can be recast into a weak formulation using a test function  $w(\cdot, t) \in H^1(\Omega(t))$  for any fixed but arbitrary  $t \in \mathbb{R}_0^+$ . Then multiplication of (2a) with the test function and integration over the domain  $\Omega(t)$  provides

$$\rho \int_{\Omega(t)} w c(x) \partial_t x d\Omega = \int_{\Omega(t)} w \nabla \cdot [\kappa(x) \nabla x] d\Omega + \int_{\Omega(t)} w \dot{W}(x) d\Omega. \quad (3)$$

Utilizing integration by parts and incorporating the mixed boundary conditions lead to the weak formulation

$$\begin{aligned}
\rho \int_{\Omega(t)} w c(x) \partial_t x d\Omega &= \int_{\Gamma(t)} w \kappa(x) \nabla x \cdot \mathbf{n} d\Gamma - \int_{\Omega(t)} \nabla w \cdot (\kappa(x) \nabla x) d\Omega \\
&+ \int_{\Omega(t)} w \dot{W}(x) d\Omega \\
&= \int_{\Gamma(t)} w \kappa_\infty(x, \mathbf{p}) [x_\infty - x] d\Gamma - \int_{\Omega(t)} \nabla w \cdot (\kappa(x) \nabla x) d\Omega \\
&+ \int_{\Omega(t)} w \dot{W}(x) d\Omega.
\end{aligned} \tag{4}$$

### 3.4. Full order system formulation using finite element approximation

The weak formulation in (4) is discretized in space with the finite element method in order to obtain ordinary differential equations (Zienkiewicz et al., 2013). For this purpose the software tool Firedrake (Rathgeber et al., 2016; Balay et al., 1997, 2019; Dalcin et al., 2011; McRae et al., 2016; Amestoy et al., 2001, 2006) is used taking into account the weak formulation (4). The resulting system can be written in matrix form

$$\mathbf{M}(\mathbf{q}, \mathbf{p}, t) \dot{\mathbf{q}} = \mathbf{K}(\mathbf{q}, \mathbf{p}, t) \mathbf{q} + \mathbf{f}(\mathbf{q}, \mathbf{p}, t), \quad t > 0, \quad \mathbf{q}(0) = \mathbf{q}_0 \in \mathbb{R}^{n_q} \tag{5}$$

with the in general sparse mass and stiffness matrices  $\mathbf{M}(\mathbf{q}, \mathbf{p}, t)$ ,  $\mathbf{K}(\mathbf{q}, \mathbf{p}, t) \in \mathbb{R}^{n_q \times n_q}$ , respectively. The inhomogeneity  $\mathbf{f}(\mathbf{q}, \mathbf{p}, t) \in \mathbb{R}^{n_q}$  results from the mixed boundary conditions (2c) and the induced heat  $\dot{W}(x(\mathbf{z}, t))$ . The explicit time dependency of the system matrices and the inhomogeneity originates from the time-varying domain  $\Omega(t)$  with boundary  $\Gamma(t)$ . The state vector  $\mathbf{q}(t) \in \mathbb{R}^{n_q}$  denotes the temperature at each node of the mesh. Local temperature measurements are summarized in the output vector  $\mathbf{y}_x(t) \in \mathbb{R}^{n_y}$  governed by

$$\mathbf{y}_x = \mathbf{C}(t) \mathbf{q}, \quad t \geq 0. \tag{6}$$

The output matrix  $\mathbf{C}(t) \in \mathbb{R}^{n_y \times n_q}$  is time-variant as the measured temperatures on the sheet metal blank and thus the mapping to the output vector change during the forming process as the sensors are usually attached to the tools so that different locations on the blank are observed during deformation. Moreover, sensors might be shadowed by the tools at some stages of the forming process.

### 3.5. Model order reduction

System (5) is composed of several thousand states and is hence not suitable for estimation and control purposes. Therefore, model order reduction is considered to systematically reduce the number of states while preserving the most important dynamics of the system in the ROM. The goal of many model order reduction techniques is to project the states of the original system  $\mathbf{q}(t)$  onto a reduced order state space by means of

$$\mathbf{q} \approx \Phi \mathbf{x}, \tag{7}$$

where  $\mathbf{x}(t) \in \mathbb{R}^{n_r}$  contains the reduced states and  $\Phi \in \mathbb{R}^{n_q \times n_r}$  is the orthonormal projection matrix.

A way to choose the basis vector of the projection matrix  $\Phi$  is POD. The POD basis vectors or POD modes, respectively, are chosen empirically using the method of snapshots (Sirovich, 1987). Let  $\mathbf{q}(t; \mathbf{u})$  denote the solution to (5) at time  $t$  for given initial state  $\mathbf{q}_0$  and process input  $\mathbf{u}$  defined in (1). Note that  $\mathbf{u}$  enters the system description by means of the parameter vector  $\mathbf{p}(\mathbf{z}, t, \mathbf{u})$  and covers also the average austenitizing temperature  $\bar{x}_\gamma$  that defines the initial state  $\mathbf{q}_0$  according to (2b). With this the snapshot matrix

$$\mathbf{X} = [\mathbf{q}(t_1; \mathbf{u}_1), \mathbf{q}(t_2; \mathbf{u}_2), \dots, \mathbf{q}(t_{n_s}; \mathbf{u}_{n_s})] \tag{8}$$



with  $\mathbf{X} \in \mathbb{R}^{n_q \times n_s}$  is defined that contains the  $n_s$  state solutions  $\mathbf{q}(t_j; \mathbf{u}_j)$  of (5) for the input  $\mathbf{u}_j$  at time  $t_j$ . The POD modes are constructed by using a singular value decomposition of the snapshot matrix

$$\mathbf{X} = \mathbf{U}\mathbf{\Sigma}\mathbf{Y}^T, \quad (9)$$

where  $\mathbf{U} \in \mathbb{R}^{n_q \times n_s}$  and  $\mathbf{Y} \in \mathbb{R}^{n_q \times n_s}$  are matrices composed of the left and right singular vectors of  $\mathbf{X}$  and  $\mathbf{\Sigma} \in \mathbb{R}^{n_s \times n_s}$  is the diagonal matrix containing the singular values  $\sigma_1 \geq \sigma_2 \geq \dots \geq \sigma_{n_s} > 0$ . The projection matrix  $\mathbf{\Phi}$  is composed of the  $n_r$  column vectors  $\mathbf{U}_j$  of  $\mathbf{U}$  corresponding to the  $n_r$  largest singular values, i.e.,

$$\mathbf{\Phi} = [\mathbf{U}_1 \quad \mathbf{U}_2 \quad \dots \quad \mathbf{U}_{n_r}]. \quad (10)$$

Since the snapshots matrix  $\mathbf{X}$  is large, a truncated singular value decomposition is performed by making use of the python library `scipy` (Virtanen et al., 2020). The singular values can also give guidance to quantify the number of basis vectors that are required to obtain a suitably accurate reconstruction of the snapshots. For this, the threshold

$$E = \frac{\sum_{i=1}^{n_r} \sigma_i}{\sum_{i=1}^{n_s} \sigma_i} < \varepsilon \quad (11)$$

is considered, where  $\varepsilon$  is a tolerance specified by the user and  $E$  is often referred to as the energy of the snapshots captured by the POD modes. Utilizing the Galerkin-projection (Benner et al., 2015), the reduced system reads

$$\mathbf{M}_r(\mathbf{x}, \mathbf{p}, t)\dot{\mathbf{x}} = \mathbf{K}_r(\mathbf{x}, \mathbf{p}, t)\mathbf{x} + \mathbf{f}_r(\mathbf{x}, \mathbf{p}, t), \quad t > 0, \quad \mathbf{x}(0) = \mathbf{x}_0 \in \mathbb{R}^{n_r} \quad (12a)$$

$$\mathbf{y}_x = \mathbf{C}_r(t)\mathbf{x}, \quad t \geq 0 \quad (12b)$$

with the transformed matrices

$$\begin{aligned} \mathbf{M}_r(\mathbf{x}, \mathbf{p}, t) &= \mathbf{\Phi}^T \mathbf{M}(\mathbf{\Phi}\mathbf{x}, \mathbf{p}, t) \mathbf{\Phi}, & \mathbf{K}_r(\mathbf{x}, \mathbf{p}, t) &= \mathbf{\Phi}^T \mathbf{K}(\mathbf{\Phi}\mathbf{x}, \mathbf{p}, t) \mathbf{\Phi}, \\ \mathbf{f}_r(\mathbf{x}, \mathbf{p}, t) &= \mathbf{\Phi}^T \mathbf{f}(\mathbf{\Phi}\mathbf{x}, \mathbf{p}, t), & \mathbf{C}_r(t) &= \mathbf{C}(t) \mathbf{\Phi}. \end{aligned}$$

The states  $\mathbf{q}(t)$  of the full system can be recovered from  $\mathbf{x}(t)$  using (7). Note that the POD method is optimal in the sense that it minimizes the least square error of the snapshot reconstruction but not that it optimally reconstructs the full model (Rathinam and Petzold, 2003). It is therefore crucial to select snapshots that excite any relevant dynamics of the system.

#### 4. State, property and disturbance estimation

During the process it is not possible to measure the entire temperature distribution  $x(\mathbf{z}, t)$  of the sheet metal blank at any time. Therefore, a state estimation concept is designed that reconstructs online the spatial-temporal temperature distribution based on the measurements  $\mathbf{y}_x(t)$ , the parameter vector  $\mathbf{p}(\mathbf{z}, t, \mathbf{u})$  depending on the solution of the mechanical subsystem and the process inputs  $\mathbf{u}(t)$  as well as the ROM (12). In addition, two modifications are introduced that reduce the computational complexity and enable us to estimate the thermal effect of the phase transformation, which is in general difficult to include into the model and to parametrize appropriately.

**Remark 3.** *In the following it is assumed that observability or detectability of the ROM is fulfilled. The proper verification of these system properties requires to study the obtained models in further detail and hence relies on the considered process and the available sensors and their placement.*

#### 4.1. Extended Kalman filter for temperature and property estimation

A widely used state and parameter estimation approach is the Kalman filter (Anderson and Moore, 2012). In the linear case it provides the optimal state estimation by the minimizing the covariance of the estimation error, i.e., the difference between the estimated state and the system (model) state under the assumptions of offset-free white process and measurement noise  $\mathbf{w}(t)$  and  $\mathbf{v}(t)$  with the positive definite covariance matrices  $\mathbf{Q}$  and  $\mathbf{R}$ , respectively. Taking these terms into account (12) reads

$$\mathbf{M}_r(\mathbf{x}, \mathbf{p}, t)\dot{\mathbf{x}} = \mathbf{K}_r(\mathbf{x}, \mathbf{p}, t)\mathbf{x} + \mathbf{f}_r(\mathbf{x}, \mathbf{p}, t) + \mathbf{w}, \quad t > 0, \quad \mathbf{x}(0) = \mathbf{x}_0 \quad (13a)$$

$$\mathbf{y}_x = \mathbf{C}_r(t)\mathbf{x} + \mathbf{v}, \quad t \geq 0. \quad (13b)$$

In view of the implementation of the estimator in a process control unit the Kalman filter is subsequently based on the discrete time version of system (12a). Taking into account a suitable discretization scheme, e.g., the explicit Euler method, Heun's method or an (explicit) Runge-Kutta scheme, formally the sampled data system

$$\mathbf{x}_k = \mathbf{F}_{k-1}(\mathbf{x}_{k-1}, \mathbf{p}_{k-1}, \mathbf{w}_{k-1}), \quad k \geq 1, \quad \mathbf{x}_0 = \mathbf{x}(0) \quad (14a)$$

$$\mathbf{y}_{x,k} = \mathbf{C}_{r,k}\mathbf{x}_k + \mathbf{v}_k \quad (14b)$$

is obtained, where  $\mathbf{x}_k = \mathbf{x}(t_k)$ ,  $\mathbf{p}_k = \mathbf{p}(t_k)$ ,  $\mathbf{w}_k = \mathbf{w}(t_k)$ ,  $\mathbf{v}_k = \mathbf{v}(t_k)$ ,  $t_k = \sum_{j=1}^k \Delta t_j$ ,  $t_0 = 0$ , and  $\Delta t_k$  is the stepsize or sampling time, respectively, which is assumed to be distributed unevenly for reasons explained below.

**Remark 4.** *The number of discretization steps for the forming process is fixed to an integer  $n_t$ . Hence each step describes a particular snapshot of the forming process determined from the LS-DYNA simulation. In other words, instead of performing a multitude of simulations for different punch speed  $v_{ps}$  and holding time  $t_h$  we address the resulting effects by adjusting the time step  $\Delta t_k$ . If the forming speed is increased, then the step size  $\Delta t_k$  is reduced. Accordingly,  $\Delta t_k$  is increased when the holding time  $t_h$  is increased. By this, the resulting effect on the temperature evolution is reflected accordingly.*

Due to the nonlinear system description an EKF is considered, which is based on the local linearization of (14) with respect to the current state estimate. For this let  $\mathbf{A}_k(\mathbf{x}_k)$  and  $\mathbf{G}_k(\mathbf{x}_k)$  denote the Jacobian matrices of  $\mathbf{F}_k(\mathbf{x}_k, \mathbf{p}_k, \mathbf{w}_k)$  with respect to  $\mathbf{x}_k$  and  $\mathbf{w}_k$ , respectively, i.e.

$$\mathbf{A}_k(\mathbf{x}_k) = \left. \frac{\partial \mathbf{F}_k(\mathbf{x}_k, \mathbf{p}_k, \mathbf{w}_k)}{\partial \mathbf{x}_k} \right|_{\mathbf{w}_k=0}, \quad \mathbf{G}_k(\mathbf{x}_k) = \left. \frac{\partial \mathbf{F}_k(\mathbf{x}_k, \mathbf{p}_k, \mathbf{w}_k)}{\partial \mathbf{w}_k} \right|_{\mathbf{w}_k=0}. \quad (15)$$

The linear Kalman filter design can be divided into two steps, namely the prediction and the update step (Anderson and Moore, 2012). This similarly extends to the EKF design by making use of the above mentioned local linearization (Gelb, 1974). In the prediction step the state estimate  $\hat{\mathbf{x}}_k^-$  is updated based on the previous state estimate  $\hat{\mathbf{x}}_{k-1}$  and parameter vector  $\mathbf{p}_{k-1}$  using (14) and the covariance matrix  $\mathbf{P}_k^-$  is computed

$$\hat{\mathbf{x}}_k^- = \mathbf{F}_{k-1}(\hat{\mathbf{x}}_{k-1}, \mathbf{p}_{k-1}, \mathbf{0}) \quad (16a)$$

$$\mathbf{P}_k^- = \mathbf{A}_{k-1}(\hat{\mathbf{x}}_{k-1})\mathbf{P}_{k-1}\mathbf{A}_{k-1}^T(\hat{\mathbf{x}}_{k-1}) + \mathbf{G}_{k-1}(\hat{\mathbf{x}}_{k-1})\mathbf{Q}\mathbf{G}_{k-1}^T(\hat{\mathbf{x}}_{k-1}). \quad (16b)$$

In the update step the state estimation is updated based on the current measurements  $\mathbf{y}_{x,k}$ . At first the Kalman gain  $\mathbf{L}_k$  is defined

$$\mathbf{L}_k = \mathbf{P}_k^- \mathbf{C}_{r,k} (\mathbf{C}_{r,k} \mathbf{P}_k^- \mathbf{C}_{r,k}^T + \mathbf{R})^{-1}, \quad (16c)$$

which is used to update state estimate and covariance matrix according to

$$\hat{\mathbf{x}}_k = \hat{\mathbf{x}}_k^- + \mathbf{L}_k (\mathbf{y}_{x,k} - \mathbf{C}_{r,k} \hat{\mathbf{x}}_k^-) \quad (16d)$$

$$\mathbf{P}_k = (\mathbf{I} - \mathbf{L}_k \mathbf{C}_{r,k}) \mathbf{P}_k^-. \quad (16e)$$



The state vector  $\hat{\mathbf{x}}_k$  of the EKF is considered as the estimate of the state  $\mathbf{x}_k$  of the ROM defined in (14). By making use of (7) the estimate

$$\hat{\mathbf{q}}_k = \Phi \hat{\mathbf{x}}_k \quad (17)$$

of the nodal temperature vector of the discrete time version of full order system (5) is obtained, which is utilized subsequently for the reconstruction of the temperature distribution in the sheet metal blank.

#### 4.2. Property estimation

Microstructural properties such as hardness of the product essentially depend on the deformation and temperature history. Based on the previously introduced state estimation approach and assuming that the deformation history is determined by the LS-DYNA simulation at a sufficient level of accuracy, then properties may be formally represented in the form

$$\mathbf{y}_p = \mathbf{h}(x, \mathbf{p}, t), \quad (18)$$

where  $\mathbf{y}_p(\mathbf{z}, t)$  summarizes the spatial-temporal property distribution. The function  $\mathbf{h}(x(\mathbf{z}, t), \mathbf{p}(\mathbf{z}, t, \mathbf{u}), t)$  may include also the temperature history, which can be represented as a convolution integral over the temperature distribution with an appropriate integral kernel. In view of the finite element approximation implying (5), the determination of the ROM (12), and the state estimation (16) the property equation (18) can be re-written in the discrete time form

$$\mathbf{y}_{p,k} = \mathbf{H}_k(\hat{\mathbf{q}}_k, \mathbf{p}_k) \quad (19)$$

with  $\mathbf{y}_{p,k}$  referring the property distribution vector at the nodes of the mesh and  $\hat{\mathbf{q}}_k$  the temperature estimation (17).

#### 4.3. Model simplification using supporting trajectories

The parameter vector  $\mathbf{p}(\mathbf{z}, t, \mathbf{u})$  in (5) is obtained from the LS-DYNA simulation, which is performed offline. Since  $\mathbf{p}(\mathbf{z}, t, \mathbf{u})$  depends on the inputs (1) by means of  $\mathbf{u}(t)$  full scenario coverage would require to numerically solve all possible combinations offline. To avoid this rather tedious procedure subsequently a so-called supporting trajectory labelled  $\bar{\mathbf{p}}(t)$  is defined, which is associated with the respective temperature trajectory  $\bar{\mathbf{q}}(t)$  to perform a linearization of the nonlinear system dynamics (5) or (12), see, e.g., [Rewieński and White \(2003\)](#). Hence under the assumption that  $\|\mathbf{q}(t) - \bar{\mathbf{q}}(t)\|_2$  is sufficiently small the model (5) is subsequently approximated by

$$\bar{\mathbf{M}}(t)\dot{\mathbf{q}} = \bar{\mathbf{K}}(t)\mathbf{q} + \bar{\mathbf{f}}(t), \quad t > 0, \quad \mathbf{q}(0) = \mathbf{q}_0 \in \mathbb{R}^{n_q} \quad (20a)$$

$$\mathbf{y}_x = \mathbf{C}(t)\mathbf{q}, \quad t \geq 0 \quad (20b)$$

with  $\bar{\mathbf{M}}(t) = \mathbf{M}(\bar{\mathbf{q}}(t), \bar{\mathbf{p}}(t), t)$ ,  $\bar{\mathbf{K}}(t) = \mathbf{K}(\bar{\mathbf{q}}(t), \bar{\mathbf{p}}(t), t)$ , and  $\bar{\mathbf{f}}(t) = \mathbf{f}(\bar{\mathbf{q}}(t), \bar{\mathbf{p}}(t), t)$ . Note that (20) does not correspond to a standard linearization using Taylor series expansion, which would imply a linearized model describing the deviation to the supporting trajectory, but rather refers to a model simplification. One particular advantage of this problem formulation is that the arising matrices, though dependent on the known variables  $(\bar{\mathbf{q}}(t), \bar{\mathbf{p}}(t))$ , can be pre-computed so that (20) can be considered as a linear time-varying system. To determine the corresponding ROM again POD can be applied as introduced in Section 3.5. This yields the ROM

$$\bar{\mathbf{M}}_r(t)\dot{\mathbf{x}} = \bar{\mathbf{K}}_r(t)\mathbf{x} + \bar{\mathbf{f}}_r(t), \quad t > 0, \quad \mathbf{x}(0) = \mathbf{x}_0 \in \mathbb{R}^{n_r} \quad (21a)$$

$$\mathbf{y}_x = \mathbf{C}_r(t)\mathbf{x}, \quad t \geq 0 \quad (21b)$$

with the matrices  $\bar{\mathbf{M}}_r(t) = \Phi^T \bar{\mathbf{M}}(t) \Phi$ ,  $\bar{\mathbf{K}}_r(t) = \Phi^T \bar{\mathbf{K}}(t) \Phi$ ,  $\bar{\mathbf{f}}_r(t) = \Phi^T \bar{\mathbf{f}}(t)$ , and  $\mathbf{C}_r(t) = \mathbf{C}(t) \Phi$  for  $\mathbf{q}(t) = \Phi \mathbf{x}(t)$ . The state and property estimation considered in Sections 4.1 and 4.2 can be identically evaluated using (21). To address the resulting errors from the model approximation as well as neglected physical effects such as phase transformation in the material a disturbance model is added and integrated into to the estimator design.

#### 4.4. Disturbance estimation

Unmodeled dynamical effects and approximation/simplification errors are subsequently subsumed in terms of an unknown disturbance vector  $\mathbf{d}(t)$  so that (5) is amended according to

$$\mathbf{M}(\mathbf{q}, \mathbf{p}, t)\dot{\mathbf{q}} = \mathbf{K}(\mathbf{q}, \mathbf{p}, t)\mathbf{q} + \mathbf{f}(\mathbf{q}, \mathbf{p}, t) + \mathbf{B}(\mathbf{q}, \mathbf{p}, t)\mathbf{d}. \quad (22)$$

The disturbance  $\mathbf{d}(t) \in \mathbb{R}^{n_d}$  can be considered as vector of power densities that act on the system and the disturbance matrix  $\mathbf{B}(\mathbf{q}, \mathbf{p}, t) \in \mathbb{R}^{n_q \times n_d}$  quantifies, where and how this power is induced. In particular  $\mathbf{B}(\mathbf{q}, \mathbf{p}, t)\mathbf{d}(t)$  can be used to represent the heat induced by phase transformation, whose mathematical description might be difficult to formulate and to parametrize, using an external model determining  $\mathbf{d}(t)$ . The main issue in this setup is the proper determination of the disturbance matrix, which will be illustrated in Section 5 for the example of a hole-flanging process by relying on physical intuition and numerical studies.

As before a ROM can be determined for (22) using POD, where the snapshot matrix (8) may be extended by varying both  $\mathbf{u}(t)$  and the disturbance vector  $\mathbf{d}(t)$  to excite the relevant system dynamics. Proceeding as before and taking into account the previously introduced approximation using a supporting trajectory the corresponding ROM can be represented as

$$\bar{\mathbf{M}}_r(t)\dot{\mathbf{x}}(t) = \bar{\mathbf{K}}_r(t)\mathbf{x}(t) + \bar{\mathbf{f}}_r(t) + \bar{\mathbf{B}}_r(t)\mathbf{d}, \quad t > 0, \quad \mathbf{x}(0) = \mathbf{x}_0 \in \mathbb{R}^{n_r}. \quad (23)$$

The unknown disturbances  $\mathbf{d}(t)$  are estimated online using the concept of Meditch and Hostetter (1973). For this, a quasi-static disturbance model is introduced in the form  $\mathbf{0} = \mathbf{A}_d\mathbf{d}(t)$  to augment (23). The term quasi-static refers to the fact that the rate of change of the disturbance can be neglected compared to the rate of change of the system state. Of course other choice can be made depending on the process characteristics. The resulting extended system reads

$$\begin{bmatrix} \bar{\mathbf{M}}_r(t) & 0 \\ 0 & \mathbf{I} \end{bmatrix} \begin{bmatrix} \dot{\mathbf{x}} \\ \dot{\mathbf{d}} \end{bmatrix} = \begin{bmatrix} \bar{\mathbf{K}}_r(t) & \bar{\mathbf{B}}_r(t) \\ 0 & \mathbf{A}_d(t) \end{bmatrix} \begin{bmatrix} \mathbf{x} \\ \mathbf{d} \end{bmatrix} + \begin{bmatrix} \bar{\mathbf{f}}_r(t) \\ \mathbf{0} \end{bmatrix} + \mathbf{w}(t), \quad t > 0, \quad \begin{bmatrix} \mathbf{x} \\ \mathbf{d} \end{bmatrix} (0) = \begin{bmatrix} \mathbf{x}_0 \\ \mathbf{d}_0 \end{bmatrix} \quad (24a)$$

$$\mathbf{y}_x = \begin{bmatrix} \mathbf{C}_r(t) & \mathbf{0} \end{bmatrix} \begin{bmatrix} \mathbf{x} \\ \mathbf{d} \end{bmatrix} + \mathbf{v}(t). \quad (24b)$$

The EKF design from Section 4.1 can then be applied to (24) with the process noise covariance matrix  $\mathbf{Q}$  amended by the one  $\mathbf{Q}_d$  of the disturbance model. This results in a combined state, property and disturbance estimation based on the augmented ROM. Note that due to the injection of the measurement and the correction of the augmented state estimate  $\hat{\mathbf{x}}_e(t) = [\hat{\mathbf{x}}^T(t), \hat{\mathbf{d}}^T(t)]^T$  by the Kalman gain the disturbance estimate  $\hat{\mathbf{d}}(t)$  is adjusted despite the assumption of quasi-stationarity of the disturbance model.

## 5. Simulation results

While the derived methods are generally applicable to multi-stage forming processes they are subsequently evaluated in simulation studies for a hole-flanging process. This process is first described and analysed before the model and approximation errors are quantified. State estimation is validated for two scenarios. First, it is evaluated based on a simulation using the finite element code Firedrake with known disturbances. Secondly, the solution of the LS-DYNA simulation involving phase transformation is used to feed the state and disturbance estimation based on the derived ROM.

### 5.1. Hole-flanging process

The validation takes place for a hole-flanging process in simulation. An illustration is shown in Figure 2. The forming process is separated in four phases: transfer (A), forming (B), holding (C), and demoulding (D). Three snapshots are taken before the forming process, during holding in the lower dead point and after the forming process at  $t = 5.2$  s,  $t = 7.6$  s and  $t = 12.1$  s, respectively. The bottom graph shows the temperature evolution at different nodes having a certain distance  $l_0$  to the centre point of the sheet metal blank obtained from a full order coupled thermo-mechanical simulation using LS-DYNA. The regions having

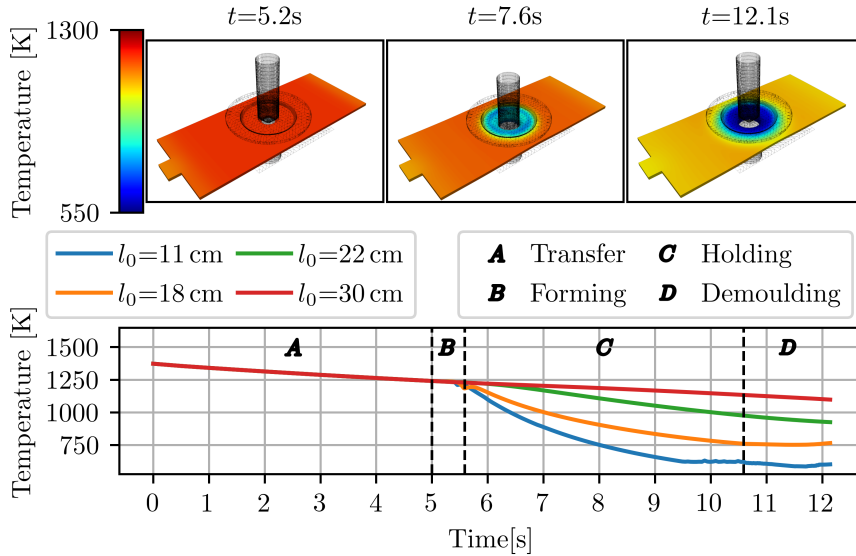


Figure 2: Temperature snapshots during the forming process obtained from a full order coupled thermo-mechanical simulation using LS-DYNA (top). Temperature evolution at four different locations with different distances  $l_0$  to the centre of the sheet metal blank (bottom). The effect of the phase transformation from austenite to martensite can be seen at approximately 10s.

tool contact ( $l_0 = 11\text{ cm}$  and  $l_0 = 18\text{ cm}$ ) cool down most, while regions which are outside the tool contact region ( $l_0 = 22\text{ cm}$  and  $l_0 = 30\text{ cm}$ ) are less affected by the forming process. At the end of the holding phase, it can be seen that the point with a distance of 11 cm stops cooling down and holds the temperature for some time. This effect is caused by the phase transformation.

The full order thermal model (5) is of dimension  $n_q = 17181$ . The input vector  $\mathbf{u}(t)$  in this process contains the punch speed  $v_{ps}$  and the austenite temperature  $\bar{x}_\gamma$ . The simulation is composed of 510 discretization steps  $n_t$  and the step sizes  $\Delta t_k$  are chosen according to Remark 4. It is assumed that pointwise temperature measurements  $\mathbf{y}_x(t)$  fixed to certain positions in the world frame are available leading to the time-variant output matrix  $\mathbf{C}(t)$  in (6). Shadowing of the sensors is not considered and measurement noise  $\mathbf{v}(t)$  with a standard deviation of 10 K is added to the signals to evaluate the performance of the state estimation. The supporting trajectory ( $\bar{\mathbf{p}}(t), \bar{\mathbf{q}}(t)$ ) is obtained from the LS-DYNA simulation with  $x_\gamma = 1273\text{ K}$  and  $v_{ps} = 80\text{ mm/s}$ .

The disturbance model is physically motivated by the phase transformation from austenite to martensite. In the given process, it is assumed that the transformation takes place simultaneously at all nodes that have tool contact, which is illustrated by the red area in Figure 3. It is assumed that there is no phase transformation in the blue area during the simulation time.

## 5.2. Model order reduction

An important step in the POD reduction method is the choice of the snapshot matrix. For the given example it is a concatenation of several full order simulations with arbitrary excitation of the disturbance  $\mathbf{d}(t)$  and varying inputs  $\mathbf{u}(t)$  to the system. The austenitizing temperature  $x_\gamma$  is varied between 1073 K and 1373 K while the punch speed  $v_{ps}$  is varied between 80 mm/s and 100 mm/s.

In Figure 4, the energy  $E$  of the snapshots that is covered by the reduced system with  $n_r$  modes as described in (11) is shown. In the given case  $n_r = 30$  modes cover over 99 % of the energy of the snapshot matrix. This assumption is also confirmed in Figure 5, where the root mean squared error (RMSE) between the full model and the reduced order model is shown for three simulations. The RMSE is thereby computed

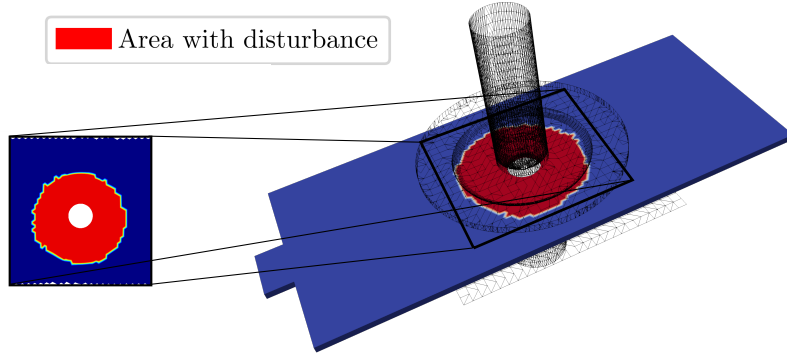


Figure 3: Red colored areas illustrate the region of phase transformation at tool contact and hence the domain addressed primarily by the disturbance model.

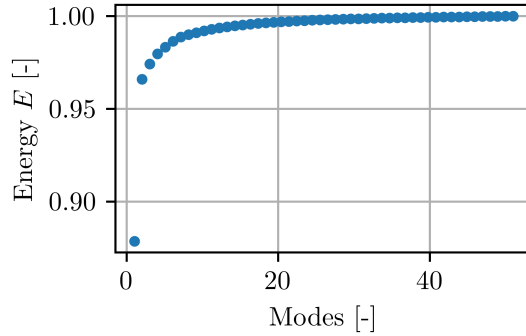


Figure 4: Approximated cumulative energy (11) covered by the POD modes.

at each time step  $k$  as

$$e_k = \frac{\int_{\Omega_k} \|\Phi \mathbf{x}_k - \mathbf{q}_k\|_2 d\Omega}{\int_{\Omega_k} d\Omega}, \quad (25)$$

where  $\Phi \mathbf{x}_k$  is the reconstructed sheet metal temperature based the reduced order states  $\mathbf{x}_k$  using (7). In the simulation with  $\bar{x}_\gamma = 1273$  K and  $v_{ps} = 80$  mm/s the error converges to 0 K as  $n_r$  is increased. This is due to the fact that this setting corresponds to the supporting trajectory  $(\bar{\mathbf{p}}(t), \bar{\mathbf{q}}(t))$  that is used for the model simplification in (21). From 9 s to 11 s a disturbance with a power density of  $1000$  W/m<sup>3</sup> is applied to the system. As this particular disturbance signal is not present in the snapshot matrix  $\mathbf{X}$ , it leads to a certain error. In the surface plots in the right column of Figure 5, which show the same subset as in Figure 3, it can be seen that the error of the disturbance arises mainly around the area with tool contact. In the second and third row, the simplification error takes effect. The RMSE with respect to a variation in  $v_{ps}$  is below 1 K in the transfer phase because the parameter trajectory is the same as in the nominal case. The RMSE rises to around 5 K in the forming phase, where the parameter and temperature trajectories deviate from the supporting trajectories. The surface plots illustrate that this error is dominant in the area of tool contact. The RMSE for a variation in  $\bar{x}_\gamma$  grows up to 20 K without the influence of disturbances. The surface plots illustrate that there is also an error outside the tool contact region which is mainly caused by the temperature dependent material properties in (2a).

The computational time for the simulation of the hole-flanging process is reduced from 33 000 s in LS-DYNA to 405 s for the full order model (5) to 0.3 s for the ROM (23) with  $n_r = 30$  states using the introduced

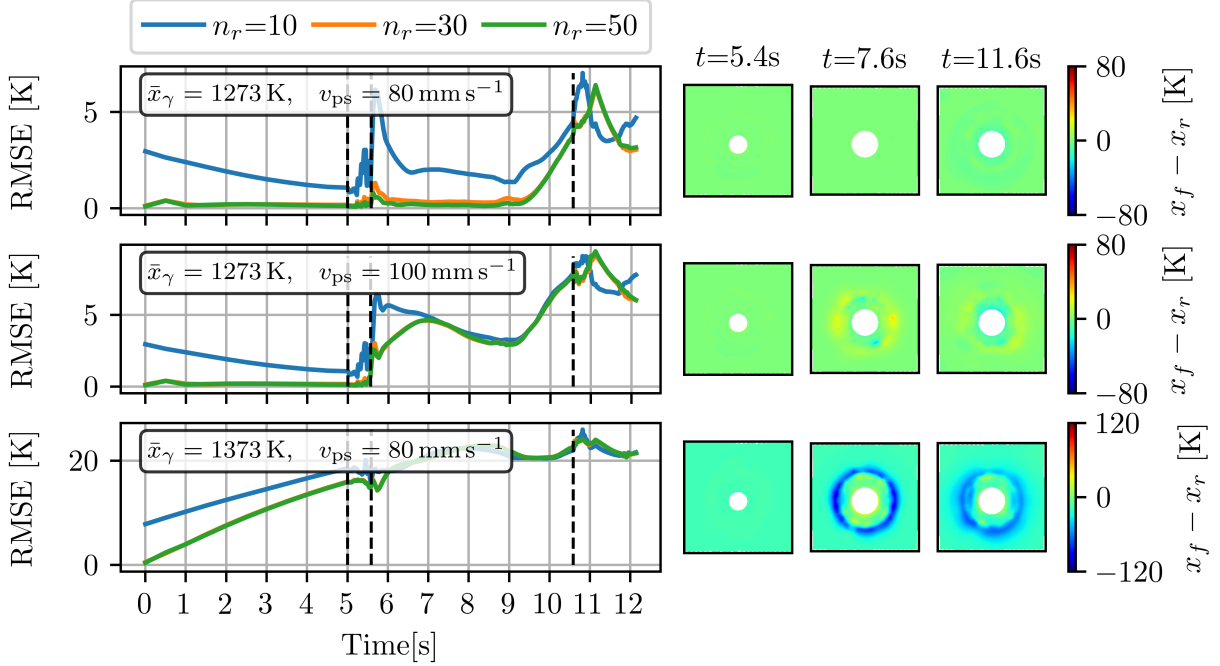


Figure 5: RMSE (25) for input variations in terms of austenitizing temperature  $\bar{x}_\gamma$  and punch speed  $v_{ps}$  (left column) and corresponding surface plots to illustrate spatial distribution of the modeling error (right column) for different dimensions  $n_r \in \{10, 30, 50\}$  of the ROM.

model simplification in terms of the supporting trajectory. This implies a reduction in computation time by a factor of 1000 from the full order model and confirms the real-time capabilities of the derived ROM. The simulation is conducted on a laptop with an Intel Core i5-8265U with 2.8 GHz.

### 5.3. State and disturbance estimation with full order thermal plant model

The state and disturbance estimation is first evaluated in combination with the full order thermal model (5). A disturbance signal  $\mathbf{d}(t)$  with a power density of  $1000 \text{ W/m}^3$  between 9s and 11s is imposed to this model, which is unknown to the EKF and needs to be reconstructed utilizing the local temperature measurements. The austenitizing temperature  $\bar{x}_\gamma$  and punch speed  $v_{ps}$  are assigned as 1373 K and 80 mm/s, respectively.

The EKF in Section 4.1 needs to be initialized with the covariance matrices of process and sensor noise. Subsequently, diagonal matrices are assumed with  $\mathbf{Q} = 10\mathbf{I}_{n_r, n_r}$  and  $\mathbf{R} = 0.1\mathbf{I}_{n_y, n_y}$ , where  $\mathbf{I}_{i,j}$  is the  $i \times j$  identity matrix. The initial state of the EKF is assigned as  $\hat{\mathbf{x}}_0 = \Phi^T \mathbf{q}_0$  and hence corresponds to the projection of the systems initial state. The initial value of the covariance matrix is chosen as  $\mathbf{P}_0 = 10\mathbf{I}_{n_r, n_r}$ . The EKF is driven by the process input  $\mathbf{u}(t)$  and  $n_y = 3$  temperature measurements summarized in the vector  $\mathbf{y}_x(t)$ . Their location is indicated in Figure 6, top right column by the crosses in the surface plots. The measurements are subsequently computed from the full order model (5). Note that sensor position is assumed spatially fixed so that the temperature of different nodes passing the measurement location due to the deformation is extracted by the matrix  $\mathbf{C}(t)$ .

The obtained estimation results are summarized in Figure 6. In the left column the temperature evolution for selected evaluation points on the sheet metal blank (corresponding to the numbers in the surface plots) are given. The first point (a) is located on a measurement point inside the disturbance region. In this case, the estimated temperature follows the true temperature without a large deviation because the disturbance estimate is chosen such that the error is minimized. In the bottom right plot, the estimated disturbance signal is compared with the applied disturbance signal. The estimate follows the true trajectory with a small

delay because a constant disturbance in the model in (24) is assumed. The second point (b) is not placed on a measurement point so that the temperature evolution is reconstructed by the EKF. Due to modeling errors the temperature is not reconstructed as good as in (a). The third node (c) is also not placed on a measurement point. However, the reconstruction is better than (b), because it is not placed within the tool contact area so that the model is more accurate. Overall the state and disturbance estimation perform well with a RMSE below 20 K, in particular in view of the comparatively low number of measurement values.

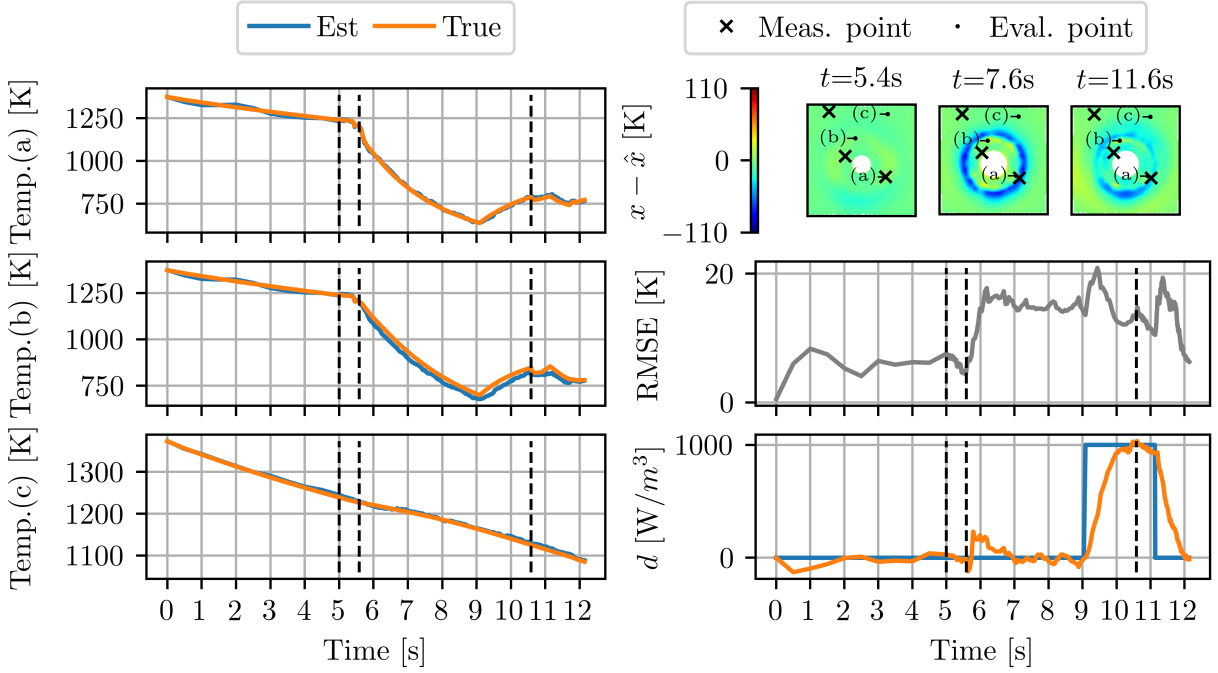


Figure 6: State and disturbance estimation using the EKF based on the augmented ROM (24) with the full order thermal model (5) of Firedrake serving as plant model for austenitizing temperature  $\bar{x}_\gamma = 1373$  K and punch speed  $v_{ps} = 80$  mm/s. Left column: comparison of estimated and simulated temperature at evaluation points; right column: location of measurement and evaluation points (top), RMSE (middle) and comparison between applied and estimated disturbance (bottom).

#### 5.4. State and disturbance estimation with thermo-mechanical LS-DYNA plant model

The state estimation is furthermore tested on the LS-DYNA simulation, where the thermal effects of the phase transformation are included by the internally used material model, so that the disturbance estimator is used to capture the respective effects. The austenitizing temperature  $x_\gamma$  and the punch speed  $v_{ps}$  are assigned as 1373 K and 80 mm/s, respectively. The sensor configuration and the initialization of the EKF correspond to those of Section 5.3.

In Figure 7 state and disturbance estimation are evaluated compared to the fully coupled thermo-mechanical LS-DYNA simulation, which is used to generate the measurement signals. As before the estimation results are more accurate for regions outside the tool contact area, subsequently represented by evaluation point (c), and at the measurement points, here evaluation point (a). In overall compared to the results of Section 5.3 the RMSE is slightly increased reaching a value of approximately 25 K without and 15 K with disturbance estimation (cf. Figure 7, right column, middle). The maximal RMSE rises when the phase transformation occurs, which is in the interval between 9 s and 11 s. The disturbance estimation (right column, bottom) herein reaches an approximate power density of  $250 \text{ W/m}^3$ . In addition, two additional peaks of  $\pm 250 \text{ W/m}^3$  emerge at the beginning of the holding phase. These are unrelated with the phase transformation and occur due to other modeling inaccuracies.



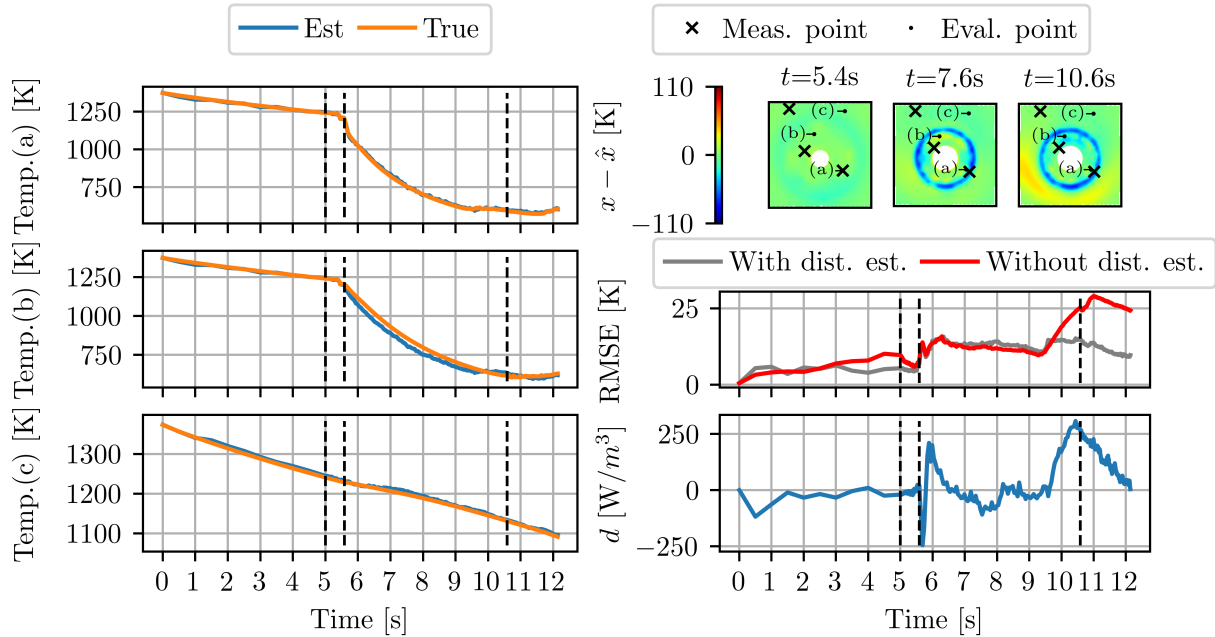


Figure 7: State and disturbance estimation using the EKF based on the augmented ROM (24) with the full coupled thermo-mechanical model of LS-DYNA serving as plant model for austenitizing temperature  $\bar{x}_\gamma = 1373$  K and punch speed  $v_{ps} = 80$  mm/s. Left column: comparison of estimated and simulated temperature at evaluation points; right column: location of measurement and evaluation points (top), RMSE with and without disturbance estimation (middle) and estimated disturbance (bottom).

## 6. Conclusion

Model-based state and disturbance estimation is developed using reduced-order models for a multi-stage hot sheet metal forming process. For this, based on the assumption of a separation between the mechanical solution and the thermal solution of the thermo-mechanical process, a nonlinear parametric model describing the spatial-temporal evolution of the temperature in the sheet metal blank during the forming process is derived taking into account a finite element approximation of the heat equation on the time-varying deforming volume. To address the high model order proper orthogonal decomposition is utilized to determine a reduced-order model capturing the essential dynamics of the thermal sub-process. Based on this system description an Extended Kalman filter is designed and augmented by a disturbance model to address modeling and approximation errors as well as neglected physical effects such as phase transformation. The computational complexity is further reduced by considering a suitable supporting trajectory which enables us to approximately consider an linear time-varying system dynamics. The performance of the state and disturbance estimation is evaluated in simulation studies for a hole-flanging process coupling the estimator with first the full order thermal model and secondly with a fully coupled thermo-mechanical simulation using LS-DYNA. The obtained results confirm the performance of the estimation approach and underline its ability to reconstruct the spatial-temporal temperature distribution in the sheet metal blank during the forming process in real-time based on only sparse local temperature measurements.

Current research considers the extension to property estimation as is already outlined schematically in this paper. Here, both the deformation history and the estimated temperature distribution starting at its initial state will be utilized in conjunction with property-related characteristic diagrams or material models to determine spatial-temporal property distributions. Both, temperature and property estimation will furthermore serve as fundamental ingredients for the model-based control of multi-stage hot sheet metal forming processes.

## Acknowledgements

The authors thank the Deutsche Forschungsgemeinschaft (DFG) for the financial support in the project 424334660 (Tekkaya/Meurer) within the Priority Program SPP2183 "Property-controlled forming processes".

## References

- Allwood, J.M., Duncan, S.R., Cao, J., Groche, P., Hirt, G., Kinsey, B., Kuboki, T., Liewald, M., Sterzing, A., Tekkaya, A.E., 2016. Closed-loop control of product properties in metal forming. *CIRP Annals - Manufacturing Technology* 65, 573–596.
- Amestoy, P., Duff, I., L'Excellent, J.Y., Koster, J., 2001. A fully asynchronous multifrontal solver using distributed dynamic scheduling. *SIAM Journal on Matrix Analysis and Applications* 23, 15–41.
- Amestoy, P., Guermouche, A., L'Excellent, J.Y., Pralet, S., 2006. Hybrid scheduling for the parallel solution of linear systems. *Parallel Computing* 32, 136–156.
- Anderson, B.D.O., Moore, J.B., 2012. *Optimal filtering*. Courier Corporation.
- Antoulas, A., 2005. *Approximation of Large-Scale Dynamical Systems*. Cambridge University Press.
- Balay, S., Abhyankar, S., Adams, M.F., Brown, J., Brune, P., Buschelman, K., Dalcin, L., Eijkhout, V., Gropp, W.D., Karpeyev, D., Kaushik, D., Knepley, M.G., May, D.A., McInnes, L.C., Mills, R.T., Munson, T., Rupp, K., Sanan, P., Smith, B.F., Zampini, S., Zhang, H., Zhang, H., 2019. *PETSc Users Manual*. Technical Report ANL-95/11 - Revision 3.11. Argonne National Laboratory.
- Balay, S., Gropp, W.D., McInnes, L.C., Smith, B.F., 1997. *Modern Software Tools in Scientific Computing*. Birkhäuser, Boston, MA. chapter Efficient Management of Parallelism in Object Oriented Numerical Software Libraries. pp. 163–20.
- Belanger, P., 2016. *Steel Innovations in Hot Stamping*. Technical Report. Gestamp.
- Belanger, P., Lage, M.L., Ruiz, L.R., Isaksson, K., 2017. New Zn Multistep Hot Stamping Innovation, in: 6th International Conference Hot Steel Metal Forming of High-Performance Steel, CHS2 2017- Proceedings, Association for Iron and Steel Technology, AISTECH. pp. 327–335.
- Benner, P., Gugercin, S., Willcox, K., 2015. A Survey of Projection-Based Model Reduction Methods for Parametric Dynamical Systems. *SIAM Rev.* 57, 483–531. doi:10.1137/130932715.
- Benosman, M., Borggaard, J., 2021. Data-driven robust state estimation for reduced-order models of 2D boussinesq equations with parametric uncertainties. *Computers & Fluids* 214, 104773. doi:10.1016/j.compfluid.2020.104773.
- Böhm, T., Meurer, T., 2017. Trajectory planning and tracking control for the temperature distribution in a deep drawing tool. *Control Engineering Practice* 64, 127–139.
- Bolzon, G., Buljak, V., 2011. An effective computational tool for parametric studies and identification problems in materials mechanics. *Comput Mech* 48, 675–687. doi:10.1007/s00466-011-0611-8.
- Dalcin, L.D., Paz, R.R., Kler, P.A., Cosimo, A., 2011. Parallel distributed computing using Python. *Advances in Water Resources* 34, 1124–1139.
- Dieck, S., Rosemann, P., Kromm, A., Halle, T., 2017. Reversed austenite for enhancing ductility of martensitic stainless steel, in: *IOP Conference Series: Materials Science and Engineering*, Institute of Physics Publishing. p. 012034.
- Gelb, A., 1974. *Applied Optimal Estimation*. MIT Press, Cambridge.
- Gracia-Escosa, E., García, I., Damborenea, J.J., Conde, A., 2017. Friction and wear behaviour of tool steels sliding against 22MnB5 steel. *Journal of Materials Research and Technology* 6, 241–250.
- Havinga, J., Mandal, P.K., 2017. Product-to-product state estimation for metal forming mass production, in: *Proceedings of Forming Technology Forum*, pp. 55–62.
- Hippchen, P., Lipp, A., Grass, H., Craighero, P., Fleischer, M., Merklein, M., 2016. Modelling kinetics of phase transformation for the indirect hot stamping process to focus on car body parts with tailored properties. *Journal of Materials Processing Technology* 228, 59–67.
- Hochholdinger, B., Hora, P., Grass, H., Lipp, A., 2011. Simulation of the press hardening process and prediction of the final mechanical material properties, in: *AIP Conference Proceedings*, pp. 618–625.
- Landgrebe, D., Pierschel, N., Alsmann, M., Schönherr, J., Polster, S., Priber, U., Schieck, F., Berndt, S., 2015. Intelligent Process Control for Press Hardening, in: Oldenburg, M., Prakash, B., Steinhoff, K. (Eds.), *5th International Conference Hot Sheet Metal Forming of High Performance Steel*, Verlag Wissenschaftliche Scripten, Toronto (CA). pp. 419–428.
- Livermore Software Technology Corporation, 2007. *LsDyna Keyword User's Manual, Volume 2*. Technical Report.
- Löbbecke, C., Hering, O., Hiegemann, L., Tekkaya, A.E., 2016. Setting mechanical properties of high strength steels for rapid hot forming processes. *Materials* 9, 229.
- Löbbecke, C., Hoppe, C., Becker, C., Tekkaya, A.E., 2015. Closed loop springback control in progressive die bending by induction heating. *International Journal of Precision Engineering and Manufacturing* 16, 2441–2449.
- Löbbecke, C., Tekkaya, A.E., 2018. Mechanisms for controlling springback and strength in heat-assisted sheet forming. *CIRP Annals* 67, 273–276.
- Martschin, J., Meya, R., Klöser, D., Meurer, T., Tekkaya, E., 2021. Control-orientated characterization of product properties during hot hole-flanging of X46Cr13 sheet material in a progressive-die. *Metals Under review*.
- McRae, A.T.T., Bercea, G.T., Mitchell, L., Ham, D.A., Cotter, C.J., 2016. Automated generation and symbolic manipulation of tensor product finite elements. *SIAM Journal on Scientific Computing* 38, 25–47.
- Meditch, J., Hostetter, G., 1973. Observers for systems with unknown and inaccessible inputs, in: *IEEE Conference on Decision and Control, IEEE*. pp. 120–124.

- Mori, K.i., Maeno, T., Tsuchiya, M., Nanya, T., 2017. Inclusion of hot stamping operations in progressive-die plate forging of tailored high strength gear part. *International Journal of Advanced Manufacturing Technology* 90, 3585–3594.
- Nikravesh, M., Naderi, M., Akbari, G.H., 2012. Influence of hot plastic deformation and cooling rate on martensite and bainite start temperatures in 22MnB5 steel. *Materials Science and Engineering A* 540, 24–29.
- Radermacher, A., Reese, S., 2014. Model reduction in elastoplasticity: Proper orthogonal decomposition combined with adaptive sub-structuring. *Comput Mech* 54, 677–687. doi:10.1007/s00466-014-1020-6.
- Rathgeber, F., Ham, D.A., Mitchell, L., Lange, M., Luporini, F., McRae, A.T., Bercea, G.T., Markall, G.R., Kelly, P.H., 2016. Firedrake: Automating the finite element method by composing abstractions. *ACM Transactions on Mathematical Software* 43.
- Rathinam, M., Petzold, L.R., 2003. A new look at proper orthogonal decomposition. *SIAM Journal on Numerical Analysis* 41, 1893–1925.
- Rewieński, M., White, J., 2003. A trajectory piecewise-linear approach to model order reduction and fast simulation of nonlinear circuits and micromachined devices. *IEEE Transactions on Computer-Aided Design of Integrated Circuits and Systems* 22, 155–170.
- Shapiro, A., 2009. Finite element modeling of hot stamping. *Steel Research International* 80, 658–664.
- Sirovich, L., 1987. Turbulence and the dynamics of coherent structures. III. Dynamics and scaling. *Quarterly of Applied Mathematics* 45, 583–590.
- Speicher, K., Steinboeck, A., Kugi, A., Wild, D., Kiefer, T., 2014. Analysis and design of an Extended Kalman Filter for the plate temperature in heavy plate rolling. *Journal of Process Control* 24, 1371–1381.
- Spittel, M., Spittel, T., 2009. Steel symbol/number: X46Cr13/1.4034: Datasheet from Landolt-Börnstein - Group VIII Advanced Materials and Technologies · Volume 2C1: "Metal Forming Data of Ferrous Alloys - deformation behaviour" in SpringerMaterials (<https://doi.org/10.1007/978-3-540-447>).
- Venturato, G., Novella, M., Bruschi, S., Ghiotti, A., Shivpuri, R., 2017. Effects of Phase Transformation in Hot Stamping of 22MnB5 High Strength Steel, in: *Procedia Engineering*, Elsevier Ltd. pp. 316–321.
- Virtanen, P., Gommers, R., Oliphant, T.E., Haberland, M., Reddy, T., Cournapeau, D., Burovski, E., Peterson, P., Weckesser, W., Bright, J., van der Walt, S.J., Brett, M., Wilson, J., Millman, K.J., Mayorov, N., Nelson, A.R., Jones, E., Kern, R., Larson, E., Carey, C.J., Polat, I., Feng, Y., Moore, E.W., VanderPlas, J., Laxalde, D., Perktold, J., Cimrman, R., Henriksen, I., Quintero, E.A., Harris, C.R., Archibald, A.M., Ribeiro, A.H., Pedregosa, F., van Mulbregt, P., Vijaykumar, A., Bardelli, A.P., Rothberg, A., Hilboll, A., Kloeckner, A., Scopatz, A., Lee, A., Rokem, A., Woods, C.N., Fulton, C., Masson, C., Häggström, C., Fitzgerald, C., Nicholson, D.A., Hagen, D.R., Pasechnik, D.V., Olivetti, E., Martin, E., Wieser, E., Silva, F., Lenders, F., Wilhelm, F., Young, G., Price, G.A., Ingold, G.L., Allen, G.E., Lee, G.R., Audren, H., Probst, I., Dietrich, J.P., Silterra, J., Webber, J.T., Slavič, J., Nothman, J., Buchner, J., Kulick, J., Schönberger, J.L., de Miranda Cardoso, J.V., Reimer, J., Harrington, J., Rodríguez, J.L.C., Nunez-Iglesias, J., Kuczynski, J., Tritz, K., Thoma, M., Newville, M., Kümmerer, M., Bolingbroke, M., Tartre, M., Pak, M., Smith, N.J., Nowaczyk, N., Shebanov, N., Pavlyk, O., Brodtkorb, P.A., Lee, P., McGibbon, R.T., Feldbauer, R., Lewis, S., Tygier, S., Sievert, S., Vigna, S., Peterson, S., More, S., Pudlik, T., Oshima, T., Pingel, T.J., Robitaille, T.P., Spura, T., Jones, T.R., Cera, T., Leslie, T., Zito, T., Krauss, T., Upadhyay, U., Halchenko, Y.O., Vázquez-Baeza, Y., 2020. SciPy 1.0: fundamental algorithms for scientific computing in Python. *Nature Methods* 17, 261–272.
- Wang, L., Zhu, B., Zhang, Y., Wang, Y., An, X., Wang, Q., 2017. A Smart Process Control Strategy for Press Hardening Production, in: Oldenburg, M., Prakash, B. (Eds.), *6th International Conference Hot Sheet Metal Forming of High Performance Steel*, Verlag Wissenschaftliche Scripten, Atlanta (USA). pp. 515—524.
- Zheng, Y., Li, S., 2011. Plant-wide temperature drop monitoring in run-out table strip cooling process. *2011 International Symposium on Advanced Control of Industrial Processes, ADCONIP 2011* , 287–292.
- Zienkiewicz, O., Taylor, R., Zhu, J.Z., 2013. *The Finite Element Method: Its Basis and Fundamentals*. 7 ed., Butterworth-Heinemann.